# Catalytic Gold-Iridium Nanoparticles as Labels for Sensitive Colorimetric Lateral Flow Assay

Zhiyuan Wei,† Keven Luciano,† and Xiaohu Xia†,‡,\*

†Department of Chemistry, University of Central Florida, Orlando, Florida 32816, United States;

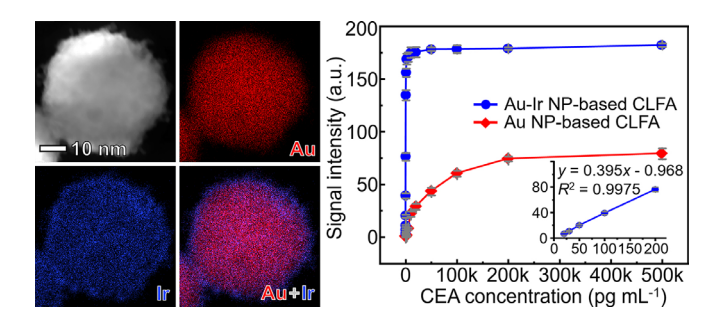
<sup>‡</sup>NanoScience Technology Center, University of Central Florida, Orlando, Florida 32816, United States.

<sup>\*</sup>Corresponding author. E-mail: Xiaohu.Xia@ucf.edu

## **Abstract**

Colorimetric lateral flow assay (CLFA, also known as test strip) is a widely used point-of-care diagnostic technology. It has been a challenge to substantially improve the detection sensitivity of CLFA without involving additional equipment and/or compromising its simplicity. In this work, we break through the detection limit barrier of CLFA by developing a type of catalytic nanoparticles (NPs) used as labels. Specifically, the NPs were engineered by coating conventional gold NPs (AuNPs) with iridium (Ir) to form an Au-Ir core-shell structure. Such Au-Ir NPs possess ultrahigh peroxidase-like catalytic activities. A single Au-Ir NP can generate up to 10<sup>7</sup> colored molecules per second by catalyzing peroxidase substrates. The strong color signal from catalysis ensures a high sensitivity of associated CLFA. The Au-Ir NP-based CLFA was successfully applied to the detection of two different cancer biomarkers that achieved limits of detection at the low picogram per milliliter level, hundreds of times lower than those of conventional AuNP-based CLFA.

# **Table of Contents**



**Keywords:** nanoparticle · lateral flow assay · catalysis · detection · biomarker

Point-of-care tests for detection of diseases are crucial to the improvement of standard of living, especially for resource-constrained countries or areas. <sup>1,2</sup> The importance and significance of pointof-care tests lie in their ability to diagnose diseases at early stages, providing patients and physicians with opportunities to make timely medical decisions. Over the past several decades, a variety of point-of-care testing technologies have been developed. Examples include lateral flow assays, <sup>3,4</sup> microfluidic-based assays, <sup>5-7</sup> pressure sensors, <sup>8-10</sup> (photo)electrochemical biosensors, <sup>11-</sup> <sup>14</sup> and many others. Among them, colorimetric lateral flow assay (CLFA) is broadly recognized as an accessible point-of-care technology because it can be used outside the laboratory, operated by a non-skilled person, and determined with naked eyes without the need of any equipment. 15,16 While CLFAs are widely used for diagnostics, 17-19 their detection sensitivity has not been significantly improved in recent years, inhibiting many critical biomedical applications. For instance, the mortality rates of infectious diseases such as Zika, Ebola, and Malaria are expected to be drastically decreased if the diseases could be detected by CLFAs at early stages with very low concentrations of related biomarkers. <sup>20-22</sup> Further, it is currently not feasible to detect selective biomarkers from a low number of cells (e.g., recovered circulating tumor cells, CTCs<sup>23</sup>), because CLFA requires orders of magnitude more analytes than can be recovered from metastasized CTCs or small tumors.

Among various colorimetric labels used in CLFA (*i.e.*, nanoscale particles pre-functionalized with bioreceptors that specifically generate visible color in the test/control lines of a CLFA test strip<sup>24</sup>), Au nanoparticles (AuNPs) with an overall spherical shape and tens of nanometers in size have been widely used for several decades owing to their superior physicochemical properties.<sup>25,26</sup> For instance, they provide intense color signal (red, in most cases) because of an phenomenon known as localized surface plasmon resonance (LSPR);<sup>27,28</sup> they can be convenienly conjugated with bioreceptors (*e.g.*, antibodies and nucleic acids) through simple electrostatic interactions or the thiol-gold chemistry;<sup>29,30</sup> and they are relatively stable because gold is an inert metal. In addition, chemical synthesis of AuNPs is simple and scaleble.

The detection sensitivity of conventional AuNP-based CLFAs is largely confined by the plasmonic activity of AuNPs, which is responsible for the generation of color signal.<sup>24</sup> A general idea to improve the 'naked eye' detection sensitivity is to amplify the plasmonics of AuNPs. The most common strategy for amplification of plasmonics is to assemble many AuNPs on a larger sized carrier particle.<sup>31,32</sup> Nevertheless, this strategy is essentially limited by the loading capacity

of a carrier, as well as the bulkiness of the resultant AuNPs-carrier complexes that may cause steric effect during the binding of bioreceptors to analytes. Another common strategy for amplification of plasmonics is to grow and thus enlarge AuNPs captured on the test line *via* gold or silver enhancement, by which particle size and thus plasmonic intensity are increased.<sup>33,34</sup> This strategy is troubled by the usage of large amounts of Au<sup>3+</sup> or Ag<sup>+</sup> ions that can adversely affect the environment and have seriously negative impacts on human health.<sup>35,36</sup>

Recently, a transformative strategy has been developed to circumvent the inherent confinement of AuNP plasmonics and thus substantially enhance the sensitivity of CLFA. 37,38 In this strategy, an innovative mechanism of color signal generation – catalysis – as an alternative to plasmonics was introduced. Specifically, conventional AuNPs were coated with Pt to form Au-Pt core-shell NPs. The Pt shell on the surface endowed the Au-Pt NPs with strong peroxidase-like catalytic activities, allowing them to generate intense color signal by catalyzing the oxidation of chromogenic substrates [*e.g.*, 3,3',5,5'-tetramethylbenzidine (TMB) and 3,3'-Diaminobenzidine (DAB)]. The color signal originated from such a catalysis process is orders of magnitude stronger than the color signal from conventional AuNP plasmonics, providing substantially enhanced detection sensitivity for CLFA. It is meaningful yet challenging to further improve the sensitivity of such catalytic NPs-based CLFA. To our knowledge, no significant improvement in sensitivity has been achieved since the initial demonstrations with Au-Pt NPs.

For this catalytic NPs-based CLFA system, the detection sensitivity is expected to be improved by enhancing the peroxidase-like catalytic activity of NPs because a more active NP can produce a stronger color signal at a lower analyte concentration.<sup>39</sup> In our previous studies,<sup>40-42</sup> we have demonstrated that metal Ir displays outstanding peroxidase-like activities. On the other hand, due to the large Ir-Ir bonding energy, Ir can grow on NP of a second noble metal to form a rough Ir shell with a large surface area,<sup>43,44</sup> which increases the catalytic activity. As inspired by these previous studies, the main idea of the present work is to coat Ir on preformed AuNPs to form Au-Ir core-shell NPs with rough surfaces. We demonstrate that such Au-Ir NPs possess maximized peroxidase-like catalytic efficiency with a catalytic constant ( $K_{cat}$ , which is defined as the maximum number of colored molecules produced per second per catalyst<sup>40,45</sup>) as high as  $10^7$  s<sup>-1</sup>. In contrast, the  $K_{cat}$  value of Au-Pt NPs with similar sizes is at the regime of  $10^6$  s<sup>-1</sup>. Such a high  $K_{cat}$  of Au-Ir NPs enable them to serve as ultrasensitive labels for CLFA. Using the detection of carcinoembryonic antigen (CEA) and prostate-specific antigen (PSA) as model biomarkers, we

demonstrated that the Au-Ir NPs offered substantially improved sensitivities for CLFA. The limit of detection (LOD) of Au-Ir NP-based CLFA was approximately 200- and 3-times lower than AuNP- and Au-Pt NP-based CLFAs, respectively, as the benchmarks.

## **RESULTS AND DISCUSSION**

**Synthesis and Characterizations.** The Au-Ir NPs were synthesized using a seed-mediated growth. In a standard synthesis, an aqueous solution of Na<sub>3</sub>IrCl<sub>6</sub> as a precursor to Ir and an aqueous solution of Na<sub>B</sub>H<sub>4</sub> as a reductant were injected slowly (1.0 mL/h, with a syringe pump) into an aqueous suspension of citrate-capped AuNPs of ~40 nm in diameter as the seeds (see the Methods section for details). Herein, ~40 nm citrate-capped AuNPs were selected as the seeds because they have been extensively used as labels for CLFA due to their optimal size and surface chemistry.<sup>24</sup> As shown by the transmission electron microscopy (TEM) image in Figure S1, the ~40 nm Au seeds had an overall spherical shape and smooth surfaces.

Figure 1a and 1b, respectively, show representative low- and high-magnification TEM images of the Au-Ir NPs that were prepared from a standard synthesis. The overall spherical shape of Au seeds was preserved after Ir growth. A careful observation indicates that the surface of the Au-Ir NPs was rough, implying Ir was grown on Au seeds towards an island or Frank-van der Merwe mode.44 Figure 1c and 1d, respectively, shows low- and high-magnification high-angle annular dark-field scanning TEM (HAADF-STEM) images of the same sample, from which the rough surfaces of Au-Ir NPs were more evident compared to the TEM images. The island growth mode of Ir and thus rough surfaces of Au-Ir NPs could be ascribed to the relatively large Ir-Ir bonding energy ( $E_{Ir-Ir} = 361 \text{ kJ/mol}$ ), which imposes large energy barrier for Ir adatoms to diffuse across the Au seed surface during synthesis. 44,46 The Au core and Ir shell structure was confirmed by the energy-dispersive X-ray (EDX) mapping and line-scanning analyses (Figure 1e and 1f). The mass ratio of Au to Ir in the Au-Ir NPs was measured to be ~10:1 by inductively coupled plasma mass spectrometry (ICP-MS). The surface properties of Au-Ir NPs were analyzed by X-ray photoelectron spectroscopy (XPS). The XPS survey spectrum taken from the Au-Ir NPs was similar to the spectrum of initial Au seeds, except for the emergence of Ir characteristic peaks (Figure 1g). This result indicated that the surface ligands on Au seeds (i.e., citrate) retained on particle surface after Ir coating, which facilitated subsequent antibody conjugation of Au-Ir NPs through attractive electrostatic interactions. <sup>17</sup> The high-resolution XPS spectra of the Ir 4f peaks

(Figure 1h) revealed that the Ir shell was primarily composed of Ir(0).<sup>43</sup>

Catalytic Activities. Peroxidase-like catalytic activities of the Au-Ir NPs was assessed through the oxidation of TMB (a typical peroxidase substrate<sup>47</sup>) by H<sub>2</sub>O<sub>2</sub> as a model catalytic reaction.<sup>40,45</sup> This reaction yielded a blue-colored product (i.e., oxidized TMB with a maximum absorption  $\lambda_{\text{max}}$ at 653 nm<sup>40</sup>) that could be conveniently tracked and quantified by a UV-vis spectrophotometer (see Figure S2). To quantify the catalytic efficiency of the Au-Ir NPs, apparent steady-state kinetic assay was conducted,  $^{40,45}$  where the particle concentration of Au-Ir NPs ([E]) was set to  $5.3 \times 10^{-1}$ <sup>14</sup> M (see details in the Methods section). A typical Michaelis-Menten curve was obtained by plotting the initial reaction velocities against TMB concentrations (Figure 2a). This curve was then converted to a double-reciprocal plot (Figure 2b),<sup>48</sup> from which the value of maximal reaction velocity  $(V_{\text{max}})$  was derived to be 5.67  $\times$  10<sup>-7</sup> M s<sup>-1</sup>. Eventually, the catalytic constant  $K_{\text{cat}}$  was calculated to be  $1.07 \times 10^7 \text{ s}^{-1}$ , according to the equation  $K_{\text{cat}} = V_{\text{max}}/[E]$ . It should be emphasized that this  $K_{\text{cat}}$  value at the regime of  $10^7$  s<sup>-1</sup> is extremely high, given that the  $K_{\text{cat}}$  values of most already reported nanostructures with peroxidase-like activities are in the range of 10<sup>3</sup>-10<sup>6</sup> s<sup>-1</sup>. <sup>49</sup> In comparison, the  $K_{\text{cat}}$  of ~40 nm AuNP seeds was measured to be ~1.0 × 10<sup>4</sup> s<sup>-1</sup> based on the kinetic assay (see Figure S3). The Kcat of Au-Pt NPs (see Figure S4) that were prepared by coating the same ~40 nm AuNP seeds with Pt was determined to be ~1.5  $\times$  10<sup>6</sup> s<sup>-1</sup> according to the kinetic assay (see Figure S5). We believe the relatively high  $K_{cat}$  of Au-Ir NPs can be ascribed to the rough surface of Ir shells that provide enlarged total surface area and more catalytically active sites. The kinetic parameters of these three types of NPs and horseradish peroxidase (HRP, a common natural peroxidase) are summarized in Table S1.

**Application in CLFA.** The Au-Ir NPs as labels were applied to CLFA, according to the principle shown in Figure 3a. After the capture of Au-Ir NPs in test/control lines of test strips, a TMB substrate treatment process was applied, which only took 5 minutes and was operated at room temperature. It should be mentioned that TMB substrate solution for membranes was applied to test strips. Owing to the presence of a precipitator, this TMB solution will develop an insoluble oxidized TMB as product. In this way, the colored product will not disperse across the membrane of test strip.<sup>37</sup> Details about the assembly of CLFA test strips and assay procedures are provided in the Methods section. For comparison, we benchmarked the performance of Au-Ir NPs in CLFA against ~40 nm citrate-capped AuNPs (which are the most commonly used labels in the CLFA industry<sup>24</sup>) by using the same antibodies and materials. The procedure of the AuNP-based CLFA

was also kept the same as the Au-Ir NP-based CLFA, except for the omission of TMB substrate treatment step.

**Detection of CEA.** Carcinoembryonic antigen (CEA, a biomarker for colorectal cancer<sup>50</sup>) standards with various concentrations in the range of 20 pg mL<sup>-1</sup> to 500 ng mL<sup>-1</sup> were detected by both Au-Ir NP- and AuNP-based CLFAs. The detection results were recorded by a digital camera (Figure 3b), which were then subject to quantification using an Adobe Photoshop software (Figure 3c).<sup>37</sup> The intensities of colored bands at the test line regions of both CLFAs increased as the concentration of CEA was increased. For the Au-Ir NP-based CLFA, blue/purple bands (resulting from oxidized TMB<sup>37</sup>) in test line regions could be visualized for strips applied with CEA standards of concentrations as low as 30 pg mL<sup>-1</sup>. In contrast, red bands (from AuNP plasmonics) in test lines of AuNP-based CLFA could only be resolved when the concentration of CEA standards was  $\geq 5$ ng mL<sup>-1</sup>. These results suggest that the naked eye detection limit of the Au-Ir NP-based CLFA is ~170 times lower than that of the AuNP-based CLFA. Figure 3c shows the calibration curves of the two CLFAs, which were generated by plotting the intensity of color at the test line against CEA concentration. Notably, the Au-Ir NP-based CLFA displayed a good linear relationship ( $R^2$  = 0.9976) in the range of 20-200 pg mL<sup>-1</sup> CEA (see the inset of Figure 3c). The limit of detection (LOD), which is defined as the 3SD method,<sup>51</sup> was calculated to be 7.8 pg mL<sup>-1</sup> for the Au-Ir NPbased CLFA. In comparison, the LOD of AuNP-based CLFA was determined to be 1.26 ng mL<sup>-1</sup>, according to its calibration curve. These results demonstrate that the Au-Ir NPs with peroxidaselike catalytic activities could enhance the sensitivity of conventional CLFA by >100 times. Such a substantial improvement is only paid by a simple, 5-minute TMB substrate treatment process. It is worth noting that the sensitivity of such an Au-Ir NP-based CLFA with a LOD at the low pg mL<sup>-1</sup> level rivals the sensitivities of some sophisticated instrument-based diagnostic techniques (e.g., enzyme-linked immunosorbent assay<sup>52</sup>). To study particle size effect, we prepared larger Au-Ir NPs (~100 nm in diameter, see Figure S6a) and applied them to CLFA of CEA. Compared to the ~40 nm Au-Ir NP-based CLFA (Figure 3b), the ~100 nm Au-Ir NP-based CLFA displayed a higher background and a lower signal-to-noise ratio (Figure S6b). Such a high background for larger particles might be due to the reduction in diffusivity and thus the retention of particles in membrane.<sup>38</sup> In the following discussions, unless otherwise stated, Au-Ir NPs refer to the ~40 nm Au-Ir NPs as shown in Figure 1.

We believe the high sensitivity of Au-Ir NP-based CLFA can be ascribed to the ultrahigh

catalytic efficiency of Au-Ir NPs, which offers highly intense color signal. To support this argument, we compared the performance of Au-Ir NPs in CLFA of CEA with Au-Pt NPs (sample in Figure S4) that had a lower peroxidase-like catalytic efficiency ( $\sim 1.5 \times 10^6 \text{ s}^{-1} \text{ versus} \sim 1.07 \times 10^7 \text{ s}^{-1}$ , in terms of  $K_{\text{cat}}$  values). These Au-Pt NPs were prepared by coating the same ~40 nm Au seeds shown in Figure S1 with Pt, which had the same surface ligands and a similar size as the Au-Ir NPs. The Au-Pt NP-based CLFA of CEA was assembled and performed in the same way as the Au-Ir NPbased CLFA, except for the substitution of Au-Ir NPs with Au-Pt NPs of the same particle amount. As shown by Figure S7a, the naked eye detection limit of the Au-Pt NP-based CLFA was 100 pg mL<sup>-1</sup>, which was ~3.3 times higher than that of Au-Ir NP-based CLFA. The LOD of Au-Pt NPbased CLFA that was determined according to its calibration curve (Figure S7b) was 3.5 times higher than the LOD of Au-Ir NP-based CLFA (27.5 pg mL<sup>-1</sup> versus 7.8 pg mL<sup>-1</sup>). We have also coated ~40 nm AuNPs with HRP (see the Methods section for details) and used the resultant AuNP-HRP conjugates as labels for CLFA of CEA. As shown by Figure S8, naked eye detection limit of AuNP-HRP-based CLFA (with TMB treatment) was ~500 pg/mL, which was much higher than that of Au-Ir NP-based CLFA. These results demonstrated that the relatively high sensitivity of Au-Ir NP-based CLFA was ascribed to the high catalytic efficiency of Au-Ir NPs.

**Detection of PSA.** To demonstrate the generality of the Au-Ir NP-based CLFA, we applied it to the detection of a second biomarker – prostate-specific antigen (PSA, a biomarker for recurrence of prostate cancer<sup>53</sup>), according to the same principle shown in Figure 3a. For comparison, AuNP-based CLFA of PSA was also performed. As shown by Figure 4a, the naked eye detection limit of the Au-Ir NP-based CLFA of PSA was as low as 10 pg mL<sup>-1</sup>. Based on the calibration curves shown in Figure 4b, the Au-Ir NP-based CLFA had a quality linear range of 5-50 pg mL<sup>-1</sup> and a LOD of 2.2 pg mL<sup>-1</sup>. In comparison, the naked eye detection limit (2 ng mL<sup>-1</sup>) and LOD (0.41 ng mL<sup>-1</sup>) of the AuNP-based CLFA of PSA were approximately 200 times higher than those of the AuNP-based CLFA. The extent of sensitivity improvement of CLFA in PSA test is similar to the case in CEA test.

**Demonstration of Clinical Use.** To evaluate the impact of biological matrices on the performance of Au-Ir NP-based CLFA, we applied it to quantifying CEA from spiked human serum samples. Serum samples were diluted 2-fold by assay buffer before spiking and loading to test strip. A CEA-free human serum sample (obtained from Sigma Aldrich) was spiked with CEA standards of five different concentrations in the range of 30-200 pg mL<sup>-1</sup>. Figure S9 shows

representative photographs taken from the Au-Ir NP-based CLFA of CEA spiked serum samples. The intensities of color signal at test lines were quantified and compared with the calibration curve shown in Figure 3c, from which the concentrations of CEA were derived. Note that the calibration curve obtained from buffer-diluted serum (see Figure S10) is similar to the calibration curve from buffer (Figure 3c). As summarized in Table 1, the analytical recoveries (defined as CEA amount measured as a percentage of the amount of CEA originally added to the serum<sup>54</sup>) of Au-Ir NP-based CLFA in detecting the five CEA spiked serum samples were in the range of 92.25-105.68%. The coefficient of variation (n = 6) for all the samples was  $\leq 8.22\%$ , suggesting a good reproducibility of the assay. These results suggested that the performance of Au-Ir NP-based CLFA was not significantly influenced by the matrices in human serum.

Finally, to demonstrate the potential clinical use of Au-Ir NP-based CLFA, we applied it to detecting PSA from patient samples that were collected by Boca Biolistics. Eight serum samples from different donors with various PSA levels were analyzed, where the concentrations of PSA in samples were pre-quantified by a commercial chemiluminescence immunoassay kit (Ortho-Clinical Diagnostics<sup>TM</sup> VITROS<sup>TM</sup> prostate-specific antigen, PSA). For quantification by the Au-Ir NP-based CLFA, the samples were diluted by assay buffer to produce signal that is located within its linear range of calibration curve (Figure 4b). Concentrations obtained from experiments were multiplied by the dilution factor to derive the PSA concentrations in original samples. As summarized by Figure 5, the detection results from Au-Ir NP-based CLFA (Figure 5a) agreed well with the data from the chemiluminescence immunoassay with a correlation coefficient  $R^2 = 0.989$  (Figure 5b). This data suggests that the Au-Ir NP-based CLFA holds great potential for application in clinical settings.

## **CONCLUSIONS**

In summary, we have demonstrated a highly sensitive CLFA. The key is to utilize Au-Ir coreshell NPs as the labels that possess strong peroxidase-like catalytic activity. The Au-Ir NPs can yield strong color signal by catalyzing chromogenic substrates. The Au-Ir NP-based CLFA was successfully applied to the detection of two different cancer biomarkers, offering low detection limits at the pg mL<sup>-1</sup> level. Compared to conventional AuNP-based CLFA, the Au-Ir NP-based CLFA was two-order-of-magnitude more sensitive. The CLFA presented in this work as a point-of-care technology is expected to find widespread uses in *in vitro* diagnostics.

## **METHODS**

Chemicals and Materials. Gold(III) chloride trihydrate (HAuCl<sub>4</sub>·3H<sub>2</sub>O, ≥99.9%), sodium citrate dihydrate (≥99%), L-ascorbic acid (AA, ≥99%), sodium hexachloroiridate(III) hydrate (Na<sub>3</sub>IrCl<sub>6</sub>·xH<sub>2</sub>O), sodium hexachloroplatinate(IV) hexahydrate (Na<sub>2</sub>PtCl<sub>6</sub>·6H<sub>2</sub>O, 98%), hydrogen peroxide solution (30 wt% in H<sub>2</sub>O), 3,3',5,5'-tetramethylbenzidine (TMB, >99%), horseradish peroxidase (HRP), TMB substrate solution for membranes, sodium acetate (NaOAc, ≥99%), acetic acid (HOAc, ≥99.7%), sodium borohydride (NaBH<sub>4</sub>), human carcinoembryonic antigen (CEA, 98%), prostate-specific antigen from human semen (PSA), bovine serum albumin (BSA,  $\geq$ 98%), potassium phosphate monobasic (KH<sub>2</sub>PO<sub>4</sub>,  $\geq$ 99%), sodium phosphate dibasic (Na<sub>2</sub>HPO<sub>4</sub>, ≥99%), potassium chloride (KCl, ≥99%), sodium chloride (NaCl, ≥99.5%), sodium azide (NaN<sub>3</sub>, ≥99.5%), sodium carbonate (Na<sub>2</sub>CO<sub>3</sub>, ≥99.5%), sucrose (≥99.5%), human serum (male AB plasma), and Tween 20 were all obtained from Sigma-Aldrich. Monoclonal mouse anti-human CEA antibody, polyclonal rabbit antihuman CEA antibody, monoclonal mouse anti-human PSA antibody, polyclonal rabbit anti-human PSA antibody were obtained from Abcam plc.. Polyclonal goat anti-mouse IgG antibody and Pierce<sup>TM</sup> protein concentrator (PES, 10K MWCO, 0.5 mL) were obtained from Thermo Fisher Scientific, Inc. Nitrocellulose (NC) membrane, glass fiber membrane, and absorbent pad were obtained from Cytiva. Polyvinyl chloride (PVC) backing card was obtained from DCN Diagnostics. Human serum samples with various PSA levels collected from different patients were purchased from Boca Biolistics LLC, Pompano Beach, Florida. All aqueous solutions were prepared using deionized (DI) water with a resistivity of 18.0 M $\Omega$ ·cm.

Instrumentations. The UV-vis spectra were recorded using an Agilent Cary 60 UV-vis spectrophotometer. Transmission electron microscopy (TEM) images were taken using a JEOL 1011 microscope operated at 200 kV. High-angle annular dark-field scanning TEM (HAADF-STEM) images, energy dispersive X-ray (EDX) mapping, and EDX line-scan profile were acquired using a FEI 200 kV Titan Themis scanning transmission electron microscope. The concentrations of Au, Ir, and Pt ions (which were obtained from the digestion of nanoparticles by aqua regia) were determined using an inductively coupled plasma mass spectroscopy (ICP-MS, Thermo Scientific iCAP RQ), which could be converted to the particle concentrations of AuNPs, Au-Ir NPs, and Au-Pt NPs once the particle sizes and shapes had been resolved by TEM imaging.<sup>37</sup> X-ray photoelectron spectroscopy (XPS) was performed on a Physical Electronics 5400 ESCA spectrometer system. The lateral flow assay test strips were prepared using a ZX1000 Dispensing Platform and a CM4000 Guillotine Cutter (BioDot Inc.). pH values of buffer solutions were measured using an Oakton pH 700 benchtop meter. Photographs of strips and samples in vials were taken using a Canon digital camera.

Synthesis of Citrate-Capped Gold Nanoparticles (AuNPs). ~40 nm, citrate-capped AuNPs were synthesized according to our previously reported two-step method.<sup>37</sup> Firstly, ~15 nm AuNPs were synthesized

as the seeds using the following procedure: a 100-mL round-bottom flask equipped with a reflux condenser containing 50 mL HAuCl<sub>4</sub> aqueous solution (0.01%, w/v) was placed in an oil bath and was heated to boiling under magnetic stirring. 2.0 mL of sodium citrate aqueous solution (1%, w/v) was then quickly injected to the flask. The solution was kept boiling and stirring for 30 min until its color turned to red. After cool-down, the ~15 nm AuNP suspension as final product was stored in dark at room temperature for future use. Secondly, the ~40 nm AuNPs were synthesized *via* a seed-mediated growth. In brief, 1.7 mL of the preformed ~15 nm AuNPs was diluted to 20 mL with DI water, and was transferred to a 50-mL round-bottom flask at room temperature under magnetic stirring. Then, 10 mL of HAuCl<sub>4</sub> aqueous solution (0.037%, w/v) and 10 mL of an aqueous solution containing AA (0.06%, w/v) and sodium citrate (0.03%, w/v) were injected separately to the flask at a rate of 12 mL/h by a syringe pump. Right after the complete injection of the two solutions, the mixture was heated to boiling in an oil bath under magnetic stirring for 30 min. Finally, the ~40 nm AuNPs as products were cooled down to room temperature, and stored in dark at room temperature for future use.

~100 nm, citrate-capped AuNPs were synthesized using a seeded growth, where the ~40 nm AuNPs mentioned above were used as seeds. Briefly, 4.0 mL of ~40 nm AuNPs was diluted to 20 mL with DI water, then transferred to a 50-mL round-bottom flask at room temperature under magnetic stirring. Then, 10 mL of HAuCl<sub>4</sub> aqueous solution (0.06%, w/v) and 10 mL of an aqueous solution containing AA (0.1%, w/v) and sodium citrate (0.05%, w/v) were injected separately to the flask at a rate of 7.5 mL/h by syringe pumps. Right after the completion of injection, the mixture was heated to boiling in an oil bath under magnetic stirring for 30 min. Finally, the ~100 nm AuNPs as products were cooled down to room temperature, and stored in dark at room temperature for future use.

**Synthesis of Au-Ir Core-Shell NPs.** For synthesis of ~40 nm Au-Ir NPs, 6.0 mL of the ~40 nm AuNPs were hosted in a 50 mL glass vial under room temperature and magnetic stirring. Then, 4.0 mL of Na<sub>3</sub>IrCl<sub>6</sub>·xH<sub>2</sub>O aqueous solution (0.5 mg/mL) and 4.0 mL of ice-cold NaBH<sub>4</sub> aqueous solution (1.0 mg/mL) were injected to the vial at a rate of 1.0 mL/h by a syringe pump. The reaction was allowed to proceed for an additional 2 hours after complete injection of the NaBH<sub>4</sub> and Na<sub>3</sub>IrCl<sub>6</sub> solutions. The products were collected by centrifugation, washed twice with water and finally re-dispersed in 6.0 mL sodium citrate aqueous solution (0.01%, w/v) for future use.

The synthetic procedure of ~100 nm Au-Ir NPs was similar to the ~40 nm Au-Ir NPs. Briefly, 6.0 mL of ~100 nm AuNPs was hosted in a 50 mL glass vial, to which 5.0 mL of Na<sub>3</sub>IrCl<sub>6</sub>·xH<sub>2</sub>O (0.5 mg/mL) and 5.0 mL of ice-cold NaBH<sub>4</sub> solution (1.5 mg/mL) were injected at a rate of 1.5 mL/h by a syringe pump. 2 h after the completion of injection, the products were washed through centrifugation and re-dispersed in 6.0 mL sodium citrate solution (0.01%, w/v).

Steady-State Kinetic Assays. All steady-state kinetic assays were carried out at room temperature in 1.0-mL cuvettes with a path length (l) of 1.0 cm using 0.2 M NaOAc/HOAc buffer (pH = 4.0) as a reaction buffer. Final particle concentration of the Au-Ir NPs in the cuvettes was set to 5.3 × 10<sup>-14</sup> M. Note the particle

concentration in this work were determined by the combination of ICP-MS analysis and TEM imaging (see the section "Instrumentations" above for details). After addition of the NPs in the reaction solution containing 2.0 M H<sub>2</sub>O<sub>2</sub> and TMB of different concentrations, the absorbance of the reaction solution at 653 nm for each sample was immediately measured as a function of time using a UV-vis spectrophotometer for 3 min (interval = 6 s). These "absorbance *versus* time" plots were then used to obtain the slope at the initial point (Slope<sub>Initial</sub>) of each reaction by conducting the first derivation using an OriginPro software. The initial reaction velocity (v) was calculated by Slope<sub>Initial</sub>/( $\varepsilon_{\text{oxTMB-653 nm}} \times I$ ), where  $\varepsilon_{\text{oxTMB-653 nm}}$  is the molar extinction coefficient of oxidized TMB at 653 nm ( $\varepsilon_{\text{oxTMB-653 nm}} = 3.9 \times 10^4 \text{ M}^{-1} \text{ cm}^{-1}$ ). The plots of v against TMB concentrations were fitted using nonlinear regression of the Michaelis-Menten equation. The apparent kinetic parameters were calculated based on the Michaelis-Menten equation  $v = V_{\text{max}} \times [S]/(K_{\text{m}} + [S])$ , where  $V_{\text{max}}$  is the maximal reaction velocity, [S] represents the concentration of TMB substrate, and  $V_{\text{max}}$  is the Michaelis constant.  $V_{\text{max}}$  could be obtained from the double reciprocal plot (or Lineweaver-Burk plot<sup>48</sup>). Finally, the catalytic constant ( $V_{\text{cat}}$ ) could be obtained from the equation:  $V_{\text{max}} = V_{\text{max}}/[E]$ , where [E] is the catalyst concentration (i.e., 5.3 × 10<sup>-14</sup> M).

Steady-state kinetic assays of ~40nm AuNPs were performed using the same procedure as Au-Ir NPs, except that the particle concentration in cuvettes was set to  $5.02 \times 10^{-12}$  M.

**Synthesis of Au-Pt Core-Shell NPs.** The Au-Pt NPs were synthesized using a seeded growth, where the ~40 nm AuNPs were used as seeds and Na<sub>2</sub>PtCl<sub>6</sub> was used as a metal precursor. Detailed procedure can be found in our previously published paper.<sup>37</sup> Herein, the mass ratio of Au to Pt in the final Au-Pt NPs was controlled to be ~6.5:1, as determined by ICP-MS measurement.

Preparation of Anti-CEA and Anti-PSA Antibodies Conjugated NPs. The Au-Ir NP-anti-CEA antibody conjugates were prepared according to our previously published work with minor modifications. <sup>37</sup> Briefly, 5.0 mL of the as-synthesized Au-Ir NP suspension was concentrated to 500 μL *via* centrifugation. Then, 50 μL of monoclonal mouse anti-human CEA antibody (2.0 mg mL<sup>-1</sup>) was added into the NP suspension. After incubation at room temperature for 30 min, the mixture was put to a refrigerator overnight at 4 °C. Subsequently, 1.0 mL of blocking solution [phosphate-buffered saline (PBS) buffer, pH 7.4, containing 10% BSA] was added to the mixture. After 1 h, the final products (*i.e.*, Au-Ir NP-anti-CEA antibody conjugates) were collected by centrifugation, washed twice with PBS, and redispersed in 1.0 mL of PBS containing 5% sucrose, 5% BSA, 0.5% Tween 20, and 0.05% NaN<sub>3</sub> for future use.

The Au-Ir NP-anti-PSA antibody conjugates were prepared using the same procedure for the Au-Ir NP-anti-CEA antibody conjugates, except that mouse anti-human CEA antibody was substituted with mouse anti-human PSA antibody of the same concentration.

The procedures for preparing the AuNP-anti-CEA/PSA antibody conjugates and the Au-Pt NP-anti-CEA/PSA antibody conjugates were the same as the procedure above, except that Au-Ir NPs were substituted with AuNPs and Au-Pt NPs, respectively, of the same particle concentration.

We have determined and controlled the average number of antibodies absorbed on individual NPs by measuring protein absorbance at OD<sub>280 nm</sub>. <sup>55,56</sup> Specifically, the total number of NPs in a conjugation reaction between NPs and antibodies was determined by ICP-MS. On the other hand, the total number of antibodies absorbed on NPs was derived by subtracting the number of antibodies in supernatant from the number of initial antibodies added to the reaction. Note, the number of free antibodies was determined by measurement of OD<sub>280 nm</sub>. <sup>55,56</sup> Eventually, the average number of antibodies absorbed on individual NPs was estimated by dividing the total number of absorbed antibodies by the number of NPs. In present study, the average numbers of antibodies conjugated to different NPs of ~40 nm in diameters were controlled to be roughly the same (~32 antibody molecules per NP).

The AuNP-HRP-anti-CEA antibody conjugates were prepared by conjugating  $\sim$ 40 nm AuNPs with HRP and monoclonal mouse anti-human CEA antibody sequentially, according to the conjugation procedure above. The amount of free HRP molecules could be estimated by measuring the absorbance of HRP-catalyzed reaction solution of TMB and  $H_2O_2$  at 653 nm ( $A_{653nm}$ ), where a calibration curve was generated by plotting  $A_{653nm}$  against the concentration of HRP.<sup>40,47</sup> The number of HRP absorbed on NPs during conjugation could be derived by subtracting the number of HRP in supernatant from the number of initial HRP added to the solution. Based on the number of AuNPs (determined by ICP-MS measurement), the average number of HRP conjugated to individual AuNPs was estimated ( $\sim$ 300 HRP molecules per NP).

Preparation of Au-Ir NP-Based CLFA Test Strips. The CLFA strips were prepared according to our previously reported procedures with minor modifications.<sup>37</sup> The Au-Ir NP-based CLFA strips consist of five major components: a sample pad, a conjugate pad, a NC membrane with a test line and a control line, an absorbent pad, and a PVC backing card (see Figure 3a). The absorbent pad and PVC backing card were utilized without any pretreatment. The sample pad was prepared by dipping a glass fiber membrane into a PBS solution containing 5% sucrose, 5% BSA, 0.5% Tween 20, and 0.05% NaN<sub>3</sub>, followed by drying out at room temperature for 4 h. The conjugate pad was prepared by dispensing the as-prepared Au-Ir NP-anti-CEA/PSA antibody conjugates onto a glass fiber membrane at a speed of 25 µL/cm using a ZX1000 Dispensing Platform, followed by drying out at room temperature for 4 h. The NC membrane with the test and control lines was prepared by separately spotting rabbit anti-human CEA/PSA antibody (1.5 mg mL<sup>-1</sup>, pre-concentrated using a Pierce<sup>TM</sup> protein concentrator, for the test line) and goat anti-mouse IgG (2.0 mg mL<sup>-1</sup> in PBS containing 0.05% NaN<sub>3</sub>, for the control line) onto the NC membrane at a jetting rate of 1.0 μL cm<sup>-1</sup> using a ZX1000 Dispensing Platform. The two lines were separated at a 5.0 mm interval. Finally, the sample pad, conjugate pad, NC membrane, and absorbent pad were sequentially assembled onto a PVC backing card with an overlap of ~2 mm. The assembled sheet was then cut into strips with a width of 4 mm. The Au-Ir NP-based CLFA strips were stored in refrigerator at -20 °C under dry condition for future use.

The procedures for preparing AuNP-based and Au-Pt NP-based CLFA strips were the same as that for the Au-Ir NP-based CLFA strips except for the substitutions of Au-Ir NP-anti-human CEA/PSA antibody conjugates with AuNP-anti-CEA/PSA antibody conjugates and Au-Pt NP-anti-CEA/PSA antibody conjugates,

respectively, of the same particle concentration.

Detection of CEA and PSA Using the Au-Ir NP-Based CLFA. 100 µL CEA or PSA standards or human

serum samples were loaded onto the sample pad of the Au-Ir NP-based CLFA strips and kept at room temperature

for ~10 min until the liquid flow was stopped. Herein, the serum was pre-diluted 2 folds by PBST buffer (i.e.,

1% BSA in PBS containing 0.05% Tween 20) prior to spiking of CEA and detection. Then, 100 μL of PBS

containing 2% Tween 20 and 100 µL of PBST were sequentially dispensed onto the sample pad and kept in order

to wash away the excess Au-Ir NP-anti-CEA/PSA antibody conjugates in the NC membrane. Then, TMB

substrate treatment process was applied, according to the following procedure: a substrate solution (i.e., a

mixture containing 6 µL of TMB substrate solution for membranes, 2 µL of 1.0 M NaOAc/HOAc buffer, pH 4.0,

and 2 μL of 1 M H<sub>2</sub>O<sub>2</sub>) was dropped onto the control and test lines of each strip. After ~2 min incubation at room

temperature, photographs of the strips were taken with a digital camera. For quantitative analysis (Figure 3c),

all the photographs were imported to a computer and converted to 8-bit grayscale images using an Adobe

Photoshop software. The arithmetic mean of pixel intensity within the test line regions was read as the color

signal intensity.

The assay procedures of the Au-Pt NP-based CLFAs of CEA and PSA were the same as that of the Au-Ir

NP-based CLFAs mentioned above. The assay procedures of the AuNP-based CLFAs of CEA and PSA were the

same as the procedures above, expect for the omission of TMB substrate treatment process. The assay procedure

of the AuNP-HRP-based CLFA of CEA was the same as that of the Au-Ir NP-based CLFAs mentioned above,

expect for the change of substrate solution to TMB substrate solution for membranes only.

ASSOCIATED CONTENT

**Supporting Information** 

The Supporting Information is available free of charge on the ACS Publications website at DOI:

XXX.

Electron microscopy images of nanostructures, photographs and UV-vis spectra of catalytic

reaction solutions, plots of kinetic assays, photographs and calibration curves of CLFAs, and a

table summarizing kinetic parameters of different catalysts.

**AUTHOR INFORMATION** 

**Corresponding Author** 

\*E-mail: xiaohu.xia@ucf.edu (X. Xia)

14

## **Notes**

The authors declare no competing financial interest.

## **ACKNOWLEDGMENTS**

This work was supported in part by a grant from the National Institute of Food and Agriculture, U.S. Department of Agriculture (2020-67021-31257), and a National Science Foundation (NSF) CAREER Award (CHE-1834874).

## REFERENCES

- (1) Yager, P.; Domingo, G. J.; Gerdes, J. Point-of-Care Diagnostics for Global Health. *Annu. Rev. Biomed. Eng.* **2008**, 10, 107-144.
- (2) Luppa, P. B.; Müller, C.; Schlichtiger, A.; Schlebusch, H. Point-of-Care Testing (POCT): Current Techniques and Future Perspectives. *TrAC Trends Anal. Chem.* **2011**, 30 (6), 887-898.
- (3) Sena-Torralba, A.; Álvarez-Diduk, R.; Parolo, C.; Piper, A.; Merkoçi, A. Toward Next Generation Lateral Flow Assays: Integration of Nanomaterials. *Chem. Rev.* **2022**, 122 (18), 14881-14910.
- (4) Khelifa, L.; Hu, Y.; Jiang, N.; Yetisen, A. K. Lateral flow assays for hormone detection. *Lab Chip* **2022**, 22 (13), 2451-2475.
- (5) Jung, W.; Han, J.; Choi, J.-W.; Ahn, C. H. Point-of-care testing (POCT) diagnostic systems using microfluidic lab-on-a-chip technologies. *Microelectron. Eng.* **2015**, 132, 46-57.
- (6) Chin, C. D.; Linder, V.; Sia, S. K. Commercialization of microfluidic point-of-care diagnostic devices. *Lab Chip* **2012**, 12 (12), 2118-2134.
- (7) Abate, M. F.; Jia, S.; Ahmed, M. G.; Li, X.; Lin, L.; Chen, X.; Zhu, Z.; Yang, C. Visual Quantitative Detection of Circulating Tumor Cells with Single-Cell Sensitivity Using a Portable Microfluidic Device. *Small* **2019**, 15 (14), 1804890.
- (8) Gong, S.; Schwalb, W.; Wang, Y.; Chen, Y.; Tang, Y.; Si, J.; Shirinzadeh, B.; Cheng, W. A wearable and highly sensitive pressure sensor with ultrathin gold nanowires. *Nat. Commun.* **2014**, 5 (1), 3132.
- (9) Yu, Z.; Tang, Y.; Cai, G.; Ren, R.; Tang, D., Paper Electrode-Based Flexible Pressure

- Sensor for Point-of-Care Immunoassay with Digital Multimeter. *Anal. Chem.* **2019,** 91 (2), 1222-1226.
- (10) Li, J.; Liu, F.; Zhu, Z.; Liu, D.; Chen, X.; Song, Y.; Zhou, L.; Yang, C. In Situ Pt Staining Method for Simple, Stable, and Sensitive Pressure-Based Bioassays. *ACS Appl. Mater. Interfaces* **2018**, 10 (16), 13390-13396.
- (11) Ronkainen, N. J.; Halsall, H. B.; Heineman, W. R. Electrochemical biosensors. *Chem. Soc. Rev.* **2010,** 39 (5), 1747-1763.
- (12) Shu, J.; Tang, D. Recent Advances in Photoelectrochemical Sensing: From Engineered Photoactive Materials to Sensing Devices and Detection Modes. *Anal. Chem.* **2020**, 92 (1), 363-377.
- (13) Zeng, R.; Gong, H.; Li, Y.; Li, Y.; Lin, W.; Tang, D.; Knopp, D. CRISPR-Cas12a-Derived Photoelectrochemical Biosensor for Point-Of-Care Diagnosis of Nucleic Acid. *Anal. Chem.* **2022**, 94 (20), 7442-7448.
- (14) Yu, Z.; Gong, H.; Xu, J.; Li, Y.; Zeng, Y.; Liu, X. Tang, D. Exploiting Photoelectric Activities and Piezoelectric Properties of NaNbO(3) Semiconductors for Point-of-Care Immunoassay. *Anal. Chem.* **2022**, 94 (7), 3418-3426.
- (15) Quesada-González, D.; Merkoçi, A. Nanoparticle-based Lateral Flow Biosensors. *Biosens. Bioelectron* **2015**, 73, 47-63.
- (16) Posthuma-Trumpie, G. A.; Korf, J.; van Amerongen, A. Lateral Flow (Immuno)Assay: Its Strengths, Weaknesses, Opportunities and Threats. A Literature Survey. *Anal. Bioanal. Chem.* 2009, 393 (2), 569-582.
- (17) Glynou, K.; Ioannou, P. C.; Christopoulos, T. K.; Syriopoulou, V. Oligonucleotide-Functionalized Gold Nanoparticles as Probes in a Dry-Reagent Strip Biosensor for DNA Analysis by Hybridization. *Anal. Chem.* **2003**, 75 (16), 4155-4160.
- (18) Kwong, G. A.; von Maltzahn, G.; Murugappan, G.; Abudayyeh, O.; Mo, S.; Papayannopoulos, I. A.; Sverdlov, D. Y.; Liu, S. B.; Warren, A. D.; Popov, Y.; Schuppan, D.; Bhatia, S. N. Mass-Encoded Synthetic Biomarkers for Multiplexed Urinary Monitoring of Disease. *Nat. Biotechnol.* **2013**, 31 (1), 63-70.
- (19) Shukla, S.; Leem, H.; Kim, M. Development of a Liposome-based Immunochromatographic Strip Assay for the Detection of Salmonella. *Anal. Bioanal. Chem.* **2011**, 401, (8), 2581-2590.
- (20) Gates, B. The Next Epidemic -- Lessons from Ebola. N. Engl. J. Med. 2015, 372 (15), 1381-

1384.

- (21) Pardee, K.; Green, A. A.; Takahashi, M. K.; Braff, D.; Lambert, G.; Lee, J. W.; Ferrante, T.; Ma, D.; Donghia, N.; Fan, M.; Daringer, N. M.; Bosch, I.; Dudley, D. M.; O'Connor, D. H.; Gehrke, L.; Collins, J. J. Rapid, Low-Cost Detection of Zika Virus Using Programmable Biomolecular Components. *Cell* **2016**, 165 (5), 1255-1266.
- (22) Feachem, R. G. A.; Phillips, A. A.; Hwang, J.; Cotter, C.; Wielgosz, B.; Greenwood, B. M.; Sabot, O.; Rodriguez, M. H.; Abeyasinghe, R. R.; Ghebreyesus, T. A.; Snow, R. W. Shrinking the Malaria Map: Progress and Prospects. *Lancet* **2010**, 376 (9752), 1566-1578.
- (23) Paterlini-Brechot, P.; Benali, N. L. Circulating Tumor Cells (CTC) Detection: Clinical Impact and Future Directions. *Cancer Lett.* **2007**, 253 (2), 180-204.
- (24) Ye, H.; Xia, X. Enhancing the Sensitivity of Colorimetric Lateral Flow Assay (CLFA) through Signal Amplification Techniques. *J. Mater. Chem. B* **2018**, 6 (44), 7102-7111.
- (25) Zhou, W.; Gao, X.; Liu, D.; Chen, X. Gold Nanoparticles for In Vitro Diagnostics. *Chem. Rev.* **2015**, 115 (19), 10575-10636.
- (26) Huang, X.; El-Sayed, M. A. Gold Nanoparticles: Optical properties and Implementations in Cancer Diagnosis and Photothermal Therapy. *J. Adv. Res.* **2010**, 1 (1), 13-28.
- (27) Eustis, S.; El-Sayed, M. A. Why Gold Nanoparticles are More Precious Than Pretty Gold: Noble Metal Surface Plasmon Resonance and Its Enhancement of the Radiative and Nonradiative Properties of Nanocrystals of Different Shapes. *Chem. Soc. Rev.* **2006**, 35 (3), 209-217.
- (28) Mayer, K. M.; Hafner, J. H. Localized Surface Plasmon Resonance Sensors. *Chem. Rev.* **2011**, 111 (6), 3828-3857.
- (29) Glomm, W. R.; Halskau, Ø.; Hanneseth, A.-M. D.; Volden, S. Adsorption Behavior of Acidic and Basic Proteins onto Citrate-Coated Au Surfaces Correlated to Their Native Fold, Stability, and pl. *J. Phys. Chem. B* **2007**, 111 (51), 14329-14345.
- (30) Love, J. C.; Estroff, L. A.; Kriebel, J. K.; Nuzzo, R. G.; Whitesides, G. M. Self-Assembled Monolayers of Thiolates on Metals as a Form of Nanotechnology. *Chem. Rev.* **2005**, 105 (4), 1103-1170.
- (31) Xu, H.; Chen, J.; Birrenkott, J.; Zhao, J. X.; Takalkar, S.; Baryeh, K.; Liu, G. Gold-Nanoparticle-Decorated Silica Nanorods for Sensitive Visual Detection of Proteins. *Anal. Chem.* **2014**, 86 (15), 7351-7359.

- (32) Shen, G.; Xu, H.; Gurung, A. S.; Yang, Y.; Liu, G. Lateral Flow Immunoassay with the Signal Enhanced by Gold Nanoparticle Aggregates Based on Polyamidoamine Dendrimer. *Anal. Sci.* **2013**, 29 (8), 799-804.
- (33) Yang, W.; Li, X.; Liu, G.; Zhang, B.; Zhang, Y.; Kong, T.; Tang, J.; Li, D.; Wang, Z. A Colloidal Gold Probe-Based Silver Enhancement Immunochromatographic Assay for the Rapid Detection of Abrin-a. *Biosens. Bioelectron* **2011**, 26 (8), 3710-3713.
- (34) Fu, E.; Liang, T.; Houghtaling, J.; Ramachandran, S.; Ramsey, S. A.; Lutz, B.; Yager, P. Enhanced Sensitivity of Lateral Flow Tests Using a Two-dimensional Paper Network Format. *Anal. Chem.* **2011**, 83 (20), 7941-7946.
- (35) Kumar, M.; Kumar, R.; Bhalla, V. Optical Chemosensor for Ag<sup>+</sup>, Fe<sup>3+</sup>, and Cysteine: Information Processing at Molecular Level. *Organic Letters* **2011**, 13 (3), 366-369.
- (36) Park, J.; Choi, S.; Kim, T.-I.; Kim, Y. Highly Selective Fluorescence Turn-On Sensing of Gold Ions by a Nanoparticle Generation/C–I Bond Cleavage Sequence. *Analyst* **2012**, 137 (19), 4411-4414.
- (37) Gao, Z.; Ye, H.; Tang, D.; Tao, J.; Habibi, S.; Minerick, A.; Tang, D.; Xia, X. Platinum-Decorated Gold Nanoparticles with Dual Functionalities for Ultrasensitive Colorimetric in Vitro Diagnostics. *Nano Lett.* **2017**, 17 (9), 5572-5579.
- (38) Loynachan, C. N.; Thomas, M. R.; Gray, E. R.; Richards, D. A.; Kim, J.; Miller, B. S.; Brookes, J. C.; Agarwal, S.; Chudasama, V.; McKendry, R. A.; Stevens, M. M. Platinum Nanocatalyst Amplification: Redefining the Gold Standard for Lateral Flow Immunoassays with Ultrabroad Dynamic Range. *ACS Nano* **2018**, 12 (1), 279-288.
- (39) Wei, Z.; Xi, Z.; Vlasov, S.; Ayala, J.; Xia, X. Nanocrystals of platinum-group metals as peroxidase mimics for in vitro diagnostics. *Chem. Commun.* **2020**, 56 (95), 14962-14975.
- (40) Xia, X.; Zhang, J.; Lu, N.; Kim, M. J.; Ghale, K.; Xu, Y.; McKenzie, E.; Liu, J.; Ye, H. Pd-Ir Core–Shell Nanocubes: A Type of Highly Efficient and Versatile Peroxidase Mimic. *ACS Nano* **2015**, 9 (10), 9994-10004.
- (41) Ye, H.; Yang, K.; Tao, J.; Liu, Y.; Zhang, Q.; Habibi, S.; Nie, Z.; Xia, X. An Enzyme-Free Signal Amplification Technique for Ultrasensitive Colorimetric Assay of Disease Biomarkers. *ACS Nano* **2017**, 11 (2), 2052-2059.
- (42) Xi, Z.; Gao, W.; Biby, A.; Floyd, A.; Xia, X. Ultrasmall Iridium Nanoparticles as Efficient Peroxidase Mimics for Colorimetric Bioassays. *ACS Appl. Nano Mater.* **2022**, 5 (5), 6089-

6093.

- (43) Xia, X.; Figueroa-Cosme, L.; Tao, J.; Peng, H.-C.; Niu, G.; Zhu, Y.; Xia, Y. Facile Synthesis of Iridium Nanocrystals with Well-Controlled Facets Using Seed-Mediated Growth. *J. Am. Chem. Soc.* **2014**, 136 (31), 10878-10881.
- (44) Xia, Y.; Xia, X.; Peng, H.-C., Shape-Controlled Synthesis of Colloidal Metal Nanocrystals: Thermodynamic versus Kinetic Products. *J. Am. Chem. Soc.* **2015**, 137 (25), 7947-7966.
- (45) Gao, L.; Zhuang, J.; Nie, L.; Zhang, J.; Zhang, Y.; Gu, N.; Wang, T.; Feng, J.; Yang, D.; Perrett, S.; Yan, X. Intrinsic Peroxidase-Like Activity of Ferromagnetic Nanoparticles. *Nat. Nanotechnol.* **2007**, 2 (9), 577-583.
- (46) Xia, X.; Xie, S.; Liu, M.; Peng, H.-C.; Lu, N.; Wang, J.; Kim Moon, J.; Xia, Y. On the Role of Surface Diffusion in Determining the Shape or Morphology of Noble-Metal Nanocrystals. *Proc. Natl. Acad. Sci. U.S.A.* **2013**, 110 (17), 6669-6673.
- (47) Josephy, P. D.; Eling, T.; Mason, R. P. The Horseradish Peroxidase-Catalyzed Oxidation of 3,5,3',5'-Tetramethylbenzidine. Free Radical and Charge-Transfer Complex Intermediates. *J. Biol. Chem.* **1982**, 257 (7), 3669-3675.
- (48) Lineweaver, H.; Burk, D. The Determination of Enzyme Dissociation Constants. *J. Am. Chem. Soc.* **1934**, 56 (3), 658-666.
- (49) Xi, Z.; Wei, K.; Wang, Q.; Kim, M. J.; Sun, S.; Fung, V.; Xia, X. Nickel–Platinum Nanoparticles as Peroxidase Mimics with a Record High Catalytic Efficiency. *J. Am. Chem. Soc.* **2021**, 143 (7), 2660-2664.
- (50) Nicholson, B. D.; Shinkins, B.; Pathiraja, I.; Roberts, N. W.; James, T. J.; Mallett, S.; Perera, R.; Primrose, J. N.; Mant, D. Blood CEA Levels for Detecting Recurrent Colorectal Cancer. *Cochrane Database Syst. Rev.* 2015, 2015 (12), Cd011134.
- (51) Armbruster, D. A.; Tillman, M. D.; Hubbs, L. M. Limit of Detection (LQD)/Limit of Quantitation (LOQ): Comparison of the Empirical and the Statistical Methods Exemplified with GC-MS Assays of Abused Drugs. *Clin. Chem.* **1994**, 40 (7), 1233-1238.
- (52) Lequin, R. M. Enzyme Immunoassay (EIA)/Enzyme-Linked Immunosorbent Assay (ELISA). *Clin. Chem.* **2005**, 51 (12), 2415-2418.
- (53) Pezaro, C.; Woo, H. H.; Davis, I. D. Prostate Cancer: Measuring PSA. *Intern. Med. J.* **2014**, 44 (5), 433-440.
- (54) Burns, D.T.; Danzer, K.; Townshend, A. Use of the Term "Recovery" and "Apparent

- Recovery" in Analytical Procedures. Pure Appl. Chem. 2002, 74, 2201-2205.
- (55) Dawes, C. C.; Jewess, P. J.; Murray, D. A. Thiophilic paramagnetic particles as a batch separation medium for the purification of antibodies from various source materials. *Anal. Biochem.* **2005**, 338 (2), 186-191.
- (56) East, D. A.; Mulvihill, D. P.; Todd, M.; Bruce, I. J. QD-antibody conjugates via carbodiimide-mediated coupling: a detailed study of the variables involved and a possible new mechanism for the coupling reaction under basic aqueous conditions. *Langmuir* **2011**, 27 (22), 13888-13896.

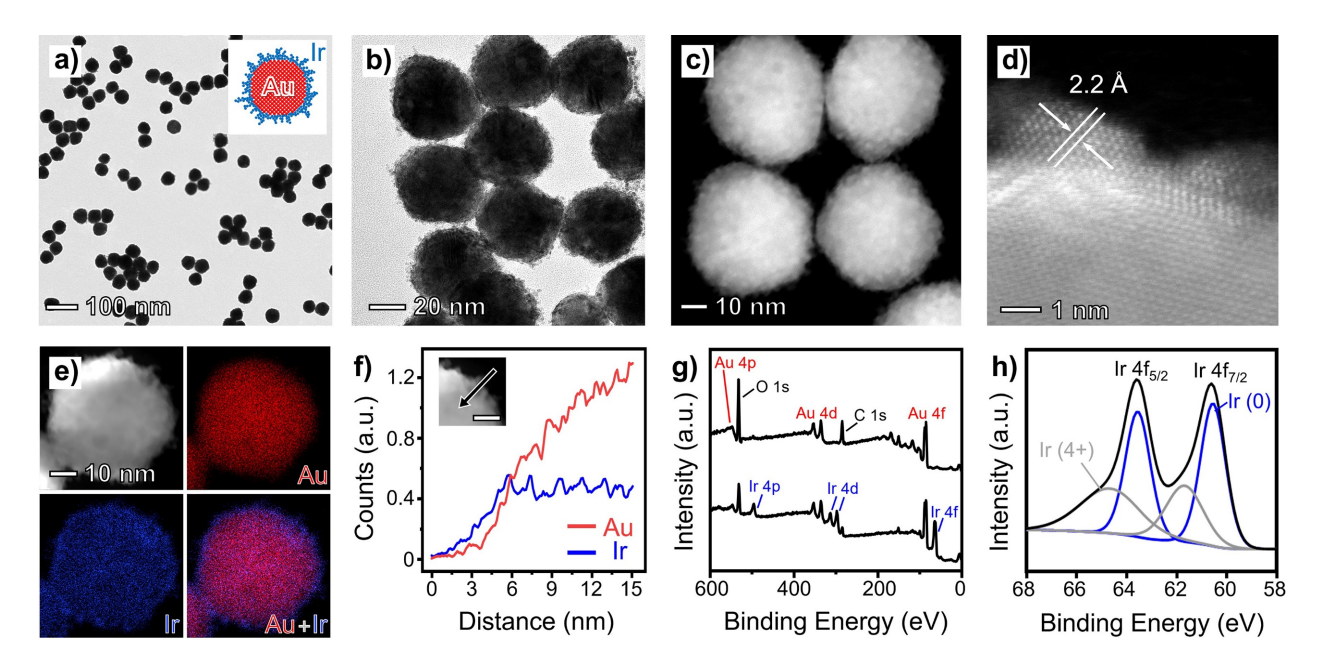


**Figure 1.** Morphological, structural, and compositional analyses of Au-Ir NPs. (a, b) Low- and high-magnification TEM images. Inset in (a) shows a 2D model of the Au-Ir NP; (c) HAADF-STEM image; (d) High-resolution HAADF-STEM image taken from an individual particle; (e) EDX mapping image of an individual particle (red = Au, blue = Ir); (f) Line-scan EDX spectra of elemental Au and Ir that were recorded from a single particle (inset; scale bar: 10 nm) along the arrow direction; (g) XPS survey spectra taken from the Au-Ir NPs and initial AuNP seeds (sample in Figure S1); (h) High-resolution XPS spectra of the Ir 4f region shown in (g).

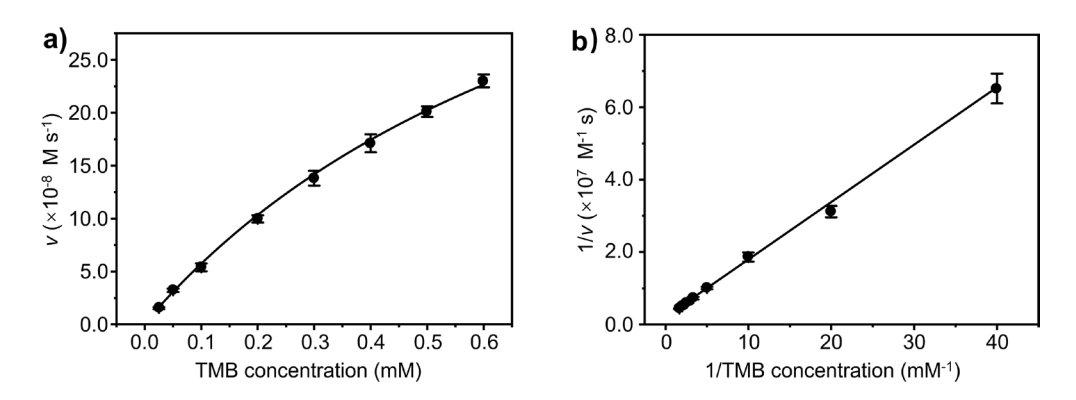


**Figure 2.** Kinetic assays of the ~40 nm Au-Ir NPs as catalysts for the oxidation of TMB by H<sub>2</sub>O<sub>2</sub>. The initial reaction velocity ( $\nu$ ) was measured in 0.2 M HOAc/NaOAc buffer solutions, pH 4.0, containing 2.0 M H<sub>2</sub>O<sub>2</sub>, 5.3 × 10<sup>-14</sup> M Au-Ir NPs, and TMB of various concentrations at room temperature. (a) Plot of  $\nu$  against TMB concentration; (b) the double-reciprocal plot that was generated from (a). Error bars denote the standard deviations of three independent measurements.

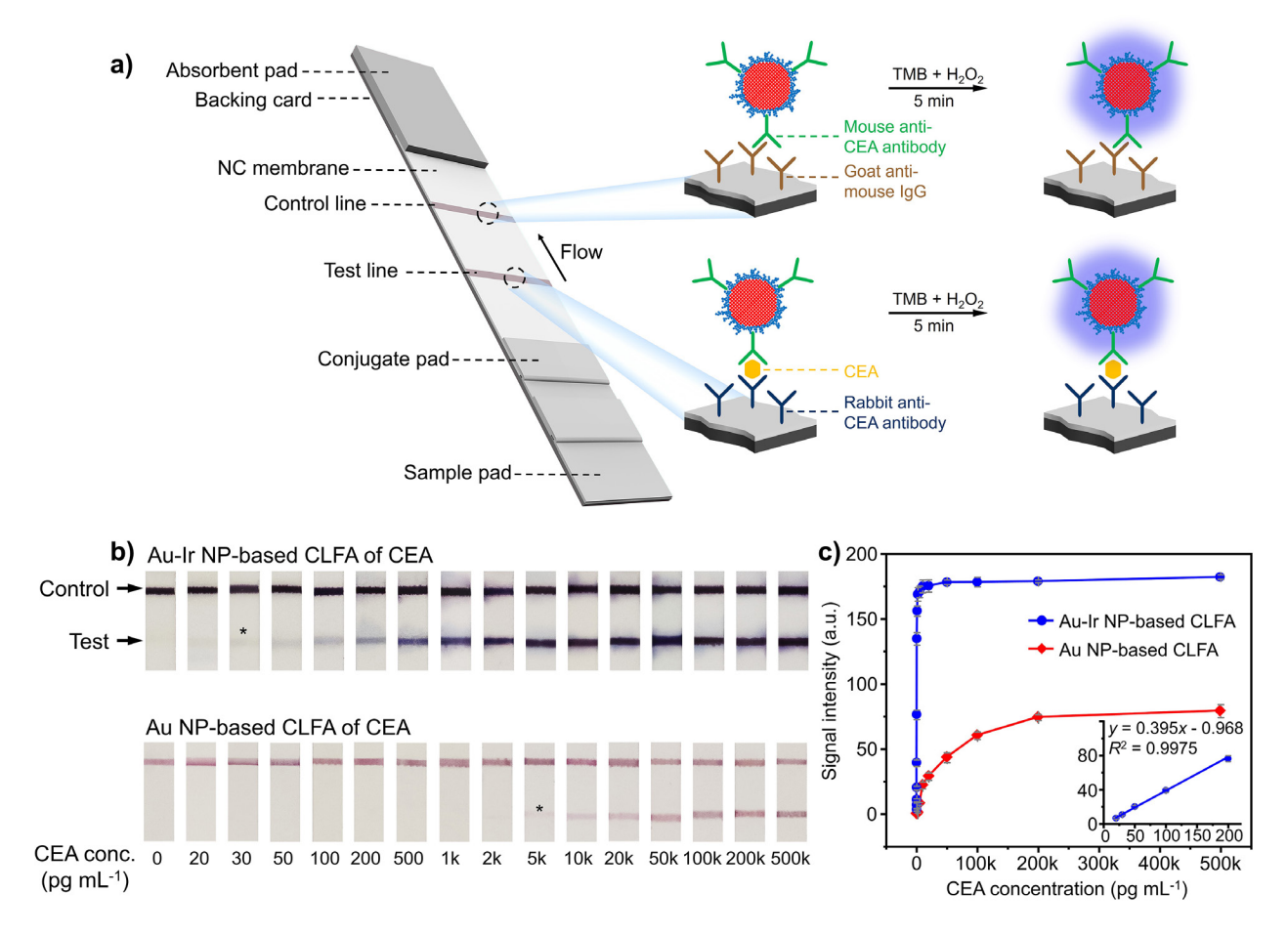


**Figure 3.** Detection of CEA using Au-Ir NP-based CLFA and conventional AuNP-based CLFA (see the Methods section for details about the preparation and operation of both CLFAs). (a) Schematics showing the principle of Au-Ir NP-based CLFA; (b) Representative photographs taken from both CLFAs of CEA standards. The asterisks (\*) indicate detection limits by the naked eyes; (c) Corresponding calibration curves of the results shown in (b). Error bars denote the standard deviations of six independent measurements. Inset of (c) shows the linear range region of the Au-Ir NP-based CLFA.

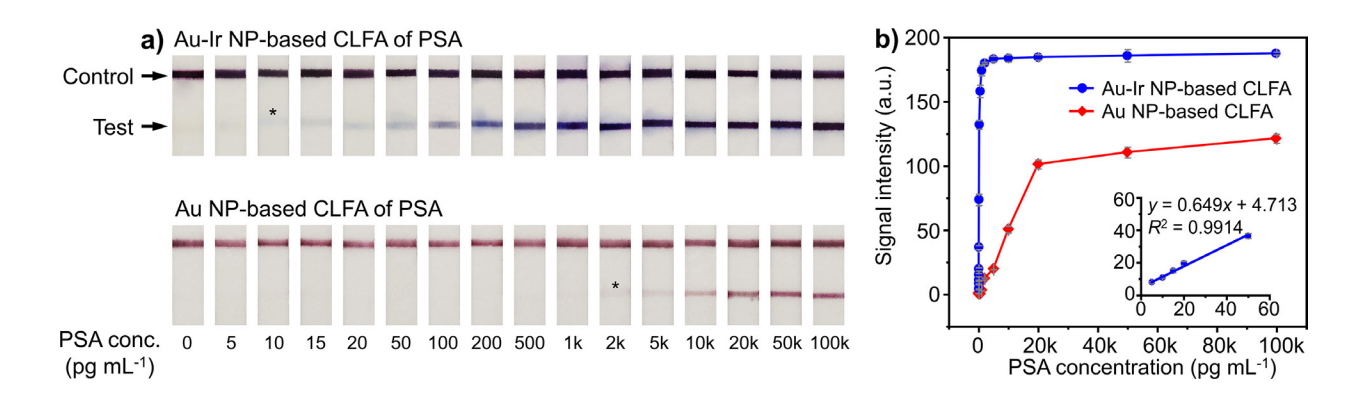


**Figure 4.** Detection of PSA using Au-Ir NP-based CLFA and conventional AuNP-based CLFA. (a) Representative photographs taken from both CLFAs of PSA standards. The asterisks (\*) indicate detection limits by the naked eyes; (b) Corresponding calibration curves of the detection results shown in (a). Error bars denote the standard deviations of six independent measurements. Inset of (b) shows the linear range region of the Au-Ir NP-based CLFA.

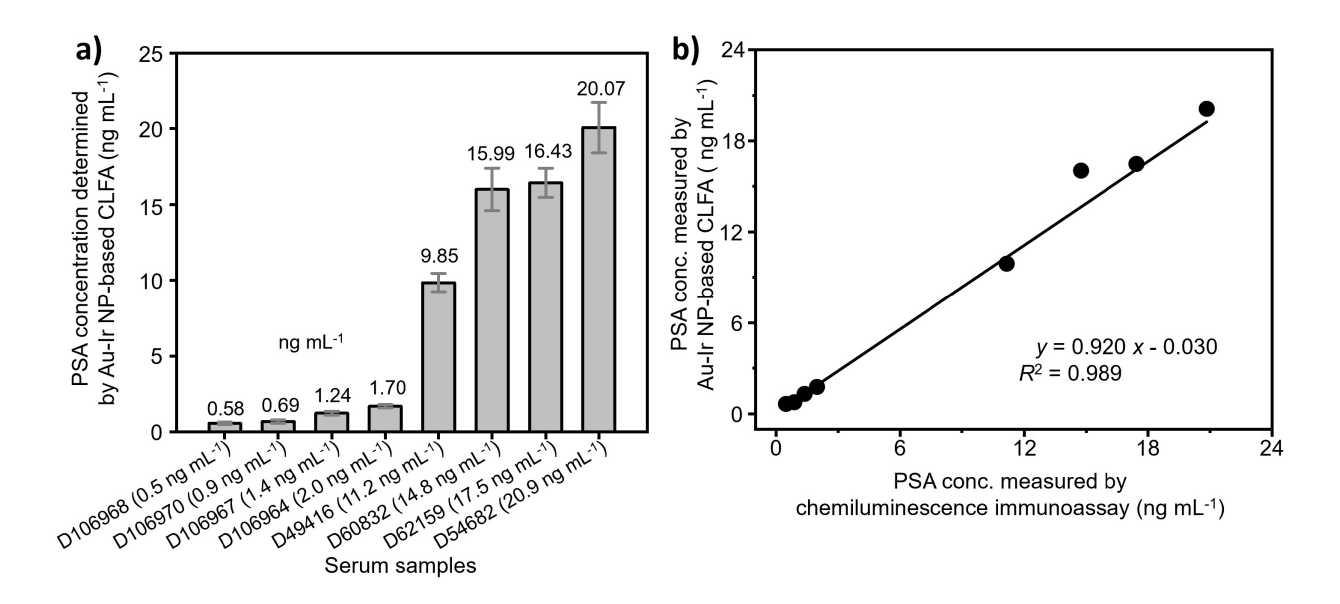


Figure 5. Au-Ir NP-based CLFA for detection of PSA in human serum samples that are collected from eight different patients. (a) bar graphs summarizing the detection results. PSA concentrations quantified by the CLFA are listed above the bars. Error bars denote the standard deviations of six independent measurements. The labels under bars indicate donor codes and corresponding PSA concentrations measured by a chemiluminescence immunoassay kit (Ortho-Clinical Diagnostics<sup>™</sup> VITROS<sup>™</sup> PSA). (b) Correlation analysis between the Au-Ir NP-based CLFA and the chemiluminescence immunoassay kit in quantifying PSA from the serum samples.

**Table 1.** The performance of Au-Ir NP-based CLFA in detecting CEA standard-spiked human serum samples.

CEA amount spiked (pg mL <sup>-1</sup> )	CEA amount measured (pg mL <sup>-1</sup> )	Coefficient of variations $(\%, n = 6)$	Recovery (%)
30	31.63	8.22	105.68
50	50.22	4.60	100.44
100	102.85	6.16	102.85
150	141.58	6.47	94.38
200	184.49	7.12	92.25